Article

Determining the AMSR-E SST Footprint from Co-located MODIS SSTs

Brahim Boussidi[1,*], Peter Cornillon[1], Gavino Puggioni[2], Chelle Gentemann[3]

[1] Graduate School of Oceanography, University of Rhode Island, 215 South Ferry Road, Narragansett, RI 02882, USA; bboussidi@uri.edu, pcornillon@me.com
[2] Department of Computer Science and Statistics, University of Rhode Island, 45 Upper College Road, Kingston 02881, RI, USA, ; gpuggioni@uri.edu
[3] Earth and Space Research, Seattle, WA, USA
[*] Correspondence: bboussidi@uri.edu

Abstract: This study was undertaken to derive and analyze the Advanced Microwave Scanning Radiometer - EOS (AMSR-E) sea surface temperature (SST) footprint associated with the Remote Sensing Systems (RSS) Level-2 (L2) product. The footprint, in this case, is characterized by the weight attributed to each 4×4 km square contributing to the SST value of a given AMSR-E pixel. High-resolution L2 SST fields obtained from the MODerate-resolution Imaging Spectroradiometer (MODIS), carried on the same spacecraft as AMSR-E, are used as the sub-resolution "ground truth" from which the AMSR-E footprint is determined. Mathematically, the approach is equivalent to a linear inversion problem, and its solution is pursued by means of a constrained least square approximation based on the bootstrap sampling procedure. The method yielded an elliptic-like Gaussian kernel with an aspect ratio ≈ 1.58, very close to the AMSR-E 6.93 GHz channel aspect ratio, ≈ 1.7. (The 6.93 GHz channel is the primary spectral frequency used to determine SST.) The semi-major axis of the estimated footprint is found to be aligned with the instantaneous field-of-view of the sensor as expected from the geometric characteristics of AMSR-E. Footprints were also analyzed year-by-year and as a function of latitude and found to be stable – no dependence on latitude or on time. Precise knowledge of the footprint is central for any satellite-derived product characterization and, in particular, for efforts to deconvolve the heavily oversampled AMSR-E SST fields and for studies devoted to product validation and comparison. A preliminarily analysis suggests that use of the derived footprint will reduce the variance between AMSR-E and MODIS fields compared to the results obtained ignoring the shape and size of the footprint as has been the practice in such comparisons to date.

Keywords: footprint, constrained Least square, Bootstrap, SST, AMSR-E, MODIS

1. Introduction

Sea surface temperature (SST), one of the ten ocean surface Essential Climate Variables (ECVs) [1], is measured from satellite-borne sensors in both the microwave portion of the electromagnetic spectrum and the infrared portion of the spectrum. The current generation of infrared instruments provide very high-resolution, $\mathcal{O}(1\,\text{km})$, SST fields contributing significantly to the study of small scale features at the ocean surface and their impact on large scale phenomena [2]. However, infrared radiometers only supply an SST estimate when they view the sea surface under cloud-free skies. This limitation severely reduces the coverage of the global oceans by infrared sensors, coverage that is strongly dependent on location and season, with some areas experiencing cloud free conditions less than 5% of the time for extended periods (months). By contrast, with the exception of regions of heavy

rainfall, the atmosphere is relatively transparent to radiation in significant portions of the microwave spectrum; i.e., SST retrievals through clouds are possible with satellite-borne instruments measuring in the microwave. The downside of microwave SST retrievals is that to achieve a reasonable accuracy, the sensor must sample a large area - the spatial resolution of these fields is generally quite course, $\mathcal{O}(60\,\text{km})$. Another important characteristic of SST fields derived from extant microwave sensors is the large overlap in pixels. As will be discussed below (Section 2.1) the sensors of interest sample approximately every 10 km in both the along- and across-track directions, while the radiometer footprint is $\mathcal{O}(45x75\,\text{km})$. These two characteristics of microwave SST retrievals, large pixel size and significant overlap in adjacent pixels, lead to some interesting problems/possibilities, one related to instrument-to-instrument comparisons and the other to enhanced resolution of the microwave SST field.

Microwave-to-Infrared SST Comparisons. Of interest to the work presented herein are two sensors, the Advanced Microwave Scanning Radiometer - EOS (AMSR-E), a microwave instrument, and the MODerate-resolution Imaging Spectroradiometer (MODIS), an infrared instrument, both carried on the National Aeronautics and Space Administration's (NASA's) Aqua satellite, launched in May 2002 [3]. The collocation of these two instruments on the same satellite platform offers the interesting possibility of providing passive microwave and infrared radiometer data, and SST fields retrieved from these data, simultaneously. A number of investigators have taken advantage of this to compare the performance of the two instruments [e.g., 4–6]. This has been done in the context of AMSR-E/MODIS matchup datasets, sets of high quality, simultaneous retrievals from the two instruments. However, in their analyses of these matchup datasets, the authors of these studies did not take into account the mismatch in the shape and size of the region sampled by each sensor. Specifically, one must average the higher resolution MODIS SSTs to the AMSR-E grid (the coarsest grid) at a similar spatial resolution in order to eliminate the MODIS high spatial variability. Given that the power spectral density of SST in the open ocean decreases linearly in log-log space with a slope of $\mathcal{O}(-2)$ [7,8], the variation of SST is a factor of 50 or more on the scale of microwave SST pixels as it is on the scale of infrared pixels. This means that SST varies significantly from one MODIS sized region in the AMSR-E pixel to another when compared to the variation within a MODIS pixel – ignoring the shape and size of the AMSR-E SST pixel will overestimate the root-mean-square difference between the two observations.

Enhanced Spatial Resolution. The AMSR-E SST retrieval algorithms developed by Remote Sensing Systems (RSS), provide SST on a 10 km grid for their L2 products and on a 25 km for their L3 product, but the region contributing to the recorded SST at each of these grid locations is, as noted above, thought to be $\mathcal{O}(45x75\,\text{km})$. This means that each point in the ocean is seen by $\mathcal{O}(35)$ pixels. It should therefore be possible to deconvolve the AMSR-E SST field yielding a true 10 km product.

The AMSR-E Footprint. In both of the cases outlined above, an accurate estimate of the shape and size of the region contributing to the AMSR-E SST retrievals will benefit the analyses. For example, use of a footprint (the weighting function mapping the temperature distribution at the ocean surface to a retrieved SST value) that is not representative of the AMSR-E SST product will result in artifacts in the differences between AMSR-E SST fields and MODIS SST, increasing the variance of the difference, as will be shown. Microwave SST data deconvolution also requires incorporation of the footprint to meet the demand for optimal reconstruction; selecting an appropriate footprint is a key preliminary step. For instance, the procedure described in [9] is based on the knowledge of the footprint measurement model.

To the best of our knowledge there are no published studies detailing the shape of the AMSR-E SST footprint, although the footprints size is commonly referred to as ranging from 50 km [10] to 58 km, with the most common reference to 56 km [2], close to the average of the axes of the 6.93 GHz footprint. The objective of the work presented herein is to determine the shape of the AMSR-E SST footprint and any dependencies that it might have on cell position, latitude and/or time. From the perspective of this study, it is important to recognize the distinction between the footprint of a given channel of an instrument and the footprint of the retrieved SST values, which may depend on more

Table 1. Nominal footprint size (Reproduced from [12, p.2-31])

Frequency (GHz)	Beam Width (°, Nominal)	Footprint (km, Across-track× Along-track)
6.925	2.2	43.2×75.4
10.65	1.5	29.4 × 51.4
18.7	0.8	15.7 × 27.4
23.8	0.9	18.1 × 31.5
36.5	0.4	8.2 × 14.4
89	0.2	3.7 × 6.5
89	0.2	3.5 × 5.9

than one spectral channel (discussed in Section 2.1), each with its own footprint, and/or on additional processing, such as averaging.

2. Data

2.1. AMSR-E

AMSR-E is a National Space Development Agency (Japan) (NASDA) instrument launched on the Aqua satellite in May 2002. It failed when its antenna stopped rotating in October 2011. AMSR-E is a dual-polarized, conical scanning, passive microwave radiometer. The wide swath (1450 km) of the instrument and the near-polar orbit in which it is flown provide near global coverage twice daily, once on the sun-side of Earth (daytime, ascending, 1330 local sun time (LST)) and once on the dark side (nighttime, descending, 0130 LST). AMSR-E, a twelve channel instrument, measures the vertical and horizontal polarization in each of six frequency bands. The AMSR-E antenna footprint, which is unique for each channel and increases with decreasing frequency, is determined by the antenna gain pattern [11]. The antenna gain pattern footprint describes how much the emissions from a particular receive direction contributes to the observed value. The Japan Aerospace Exploration Agency (JAXA) provides measured antenna patterns for the AMSR-E sensor at all center frequencies. The nominal size of the footprint for each of the spectral bands is reproduced from [12] in Table 1. For additional details with regard to the footprint, please see [13]. As noted in the introduction, there is likely a difference between the SST footprint and the footprint of the primary spectral channel contributing to the retrieval.

The scan geometry of the instrument in orbit is shown in Fig. 1. The satellite orbit height is 705 km, the ground incidence angle is 55°, and the observation angle range is from –61 °to +61 °. In one scan, AMSR-E samples 243 cell footprints for each of the frequency bands except for the 89 GHz band, for which it samples at twice the frequency.

In this study, we use SST fields obtained with version-7 (v7) of the AMSR-E algorithm developed by RSS. This algorithm simultaneously determines water vapor, cloud liquid water, precipitation, sea surface wind speed (WS) and SST using brightness temperature measurements from all spectral channels except for those at 89 GHz. SST, the variable of interest here, is derived primarily from the 6.93 GHz channel. As shown in Table 1, the ground resolution of the 6.93 GHz channel is approximately 75 km in the direction defined by a vector from the pixel to the nadir point of the satellite and approximately 43 km normal to this vector [12]. Thus, the retrieved SST is of coarse spatial resolution. The distance between adjacent observations for all channels, except those of 89 GHz, is approximately 10 km across-track and 10 km along-track [11]; i.e., the 6.93 GHz channel is substantially oversampled, with the remaining channels being less so. (Note that because the axis of the scanner is tilted, a scan-line describes an approximate circle on the Earth's surface so, as one moves away from nadir, the across-track direction is not orthogonal to the along-track direction.) To work simultaneously with all spectral channels, the RSS retrieval algorithm resamples the brightness
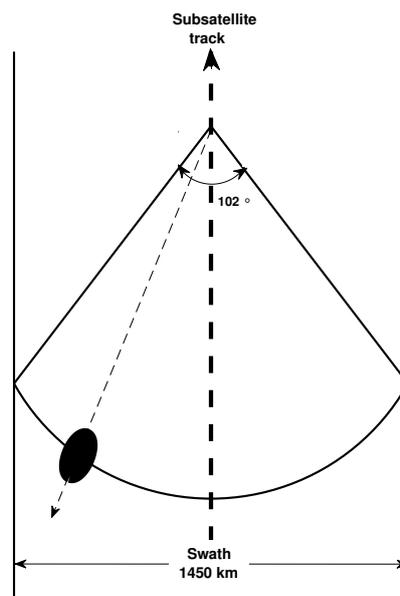
Figure 1. The scan geometry of the Advanced Microwave Scanning Radiometer - EOS (AMSR-E). The dark ellipse schematically illustrates the Advanced Microwave Scanning Radiometer - EOS (AMSR-E) footprint.

118 temperatures for each of the spectral channels to match the resolution of the 6.93 GHz channel [14].
119 The SST is then retrieved using a physically based two-stage regression algorithm that expresses SST
120 in terms of the resampled brightness temperatures (see the Appendix of [2] for an overview of the
121 AMSR-E SST retrieval algorithm). The retrieved values for each grid point are then averaged over five
122 along-track pixels, two on each side of the pixel of interest.

123   Errors in the AMSR-E SST retrievals result primarily from scattering due to rain, sidelobe
124 contamination due to proximity to land and/or sea ice, radio frequency interference (RFI), sunglint,
125 wind speed >20 m/s and proximity to the edge of the swath. Pixels flagged for any of these
126 conditions were excluded from the analysis.

127 *2.2. MODIS*

128   MODIS is also carried on the Aqua satellite. This infrared instrument has several spectral channels
129 in the thermal infrared allowing for high quality, high resolution SST retrievals. The L2 MODIS SST
130 product used here is derived from the far-infrared bands, which have a resolution of approximately
131 1 km at nadir. For this study, we used the MODIS SST product obtained from the NASA Ocean Biology
132 Processing Group (OBPG) [15]. This product is based on the nonlinear SST (NLSST) algorithm [16,17].
133 Various factors contribute to errors in the retrievals, with atmospheric water vapor and/or clouds
134 thought to be the primary contributors to statistical measures of the uncertainty of L2 products [18].
135 (For simplicity, we refer to contamination from either of these sources as 'cloud contamination'.)
136 Because of the impact of clouds on SST values retrieved from IR measurements, significant effort is
137 devoted to flagging the presence of suspect, generally cloud contaminated, pixels. Specifically, a
138 quality level from 0 to 4 was assigned to each MODIS SST pixel. The higher the quality level, the poorer
139 the quality of the pixel. In this study, we used only quality level 0 data; i.e., the 'best' quality retrievals.
140 However, some contaminated pixels are still flagged as quality 0; i.e., a Type II misclassification error
141 based on the statistical hypothesis that the pixel is cloud free. Type I errors, clear pixels being flagged
142 as 'bad', occur as well but these only have a marginal impact on the uncertainty of the product.

143   The OBPG retrieval algorithm computes one set of SST fields for the daytime hours, based on the
144 two channels in the 10 to 12 μm portion of the spectrum (referred to here as the 11 μm algorithm), and
145 two sets of nighttime fields, one based on the two thermal-infrared channels and the other making

use of these channels together with the water vapor channel. We used SST fields obtained with the 11 μm algorithm for this study.

3. Methodology

3.1. Matchup dataset

The starting point for this work was an approximately four million point AMSR-E–MODIS SST matchup dataset. A matchup is defined as a nighttime L2 AMSR-E SST pixel, meeting the quality criteria specified in section 2.1, and a 101×125 MODIS L2 SST pixel region, centered on the AMSR-E pixel, for which 90% of the MODIS pixels were classified as clear – quality 0. The 101 element dimension of the MODIS regions selected is defined parallel to the MODIS across-track direction. The 125 element dimension is in the along-track direction. The size of the MODIS region was selected so that it would include all pixels contributing to the radiances of all bands used to determine the AMSR-E SST. As noted in Section 2.1, the AMSR-E antenna scans at an off-nadir angle (47.5° from nadir) with each scan line defining an approximately circular section (Fig. 1). Samples, numbered from -122 to 122, with 0 corresponding to nadir, are taken approximately every 10 km along this circular section as shown in Fig. 2. Important for this discussion, the semi-major axes of the footprints of the AMSR-E spectral bands (AMSR-E spectral footprints hereafter) are parallel to the vector from the nadir position of the satellite to the pixel of interest. By contrast, MODIS scans along lines passing through nadir, lines that are approximately normal to the nadir track. This results in an angle, which depends on cell position, between the semi-major axis of the AMSR-E spectral footprints and the MODIS scan geometry. Fig. 3 shows this angle at each cell position.

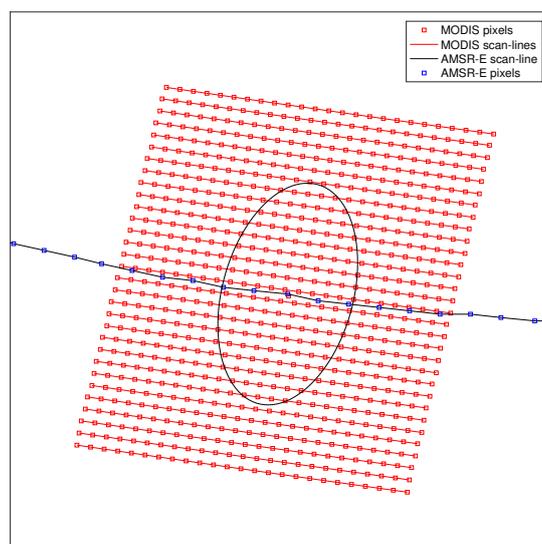**Figure 2.** Example of matchup data.

Note that a matchup could also have been defined with one of the axes perpendicular to the AMSR-E scan line at the pixel of interest, however, this would have entailed a more complex subsampling of the MODIS data. Furthermore, it was not known at the outset whether or not the AMSR-E SST footprint would be aligned with the AMSR-E spectral footprints.

Gaps, if they exist in the MODIS patch, were filled by solving the Laplace equation with Dirichlet boundary conditions using the MATLAB routine *roifill*. Following this step, the full resolution MODIS data were degraded to lower resolution (for computational efficiency, as will be shown in Section 3.2) by averaging the initial fields over 4 x 4 pixels (≈ 4km resolution at nadir). This resulted in a total of 775 (25x31) MODIS SST measurements. Fig. 4 shows the global distribution of the matchup data. This
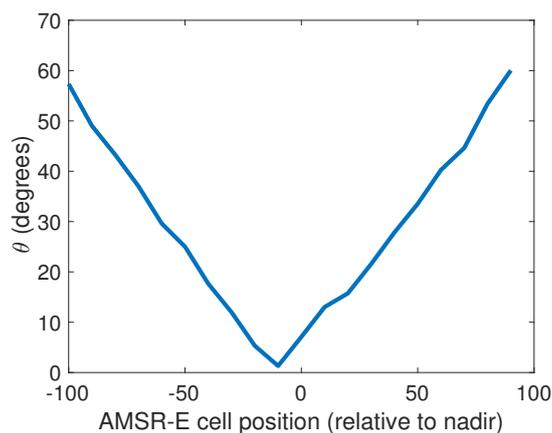
Figure 3. Relative angle between AMSR-E and MODIS scans as a function of AMSR-E cell position.
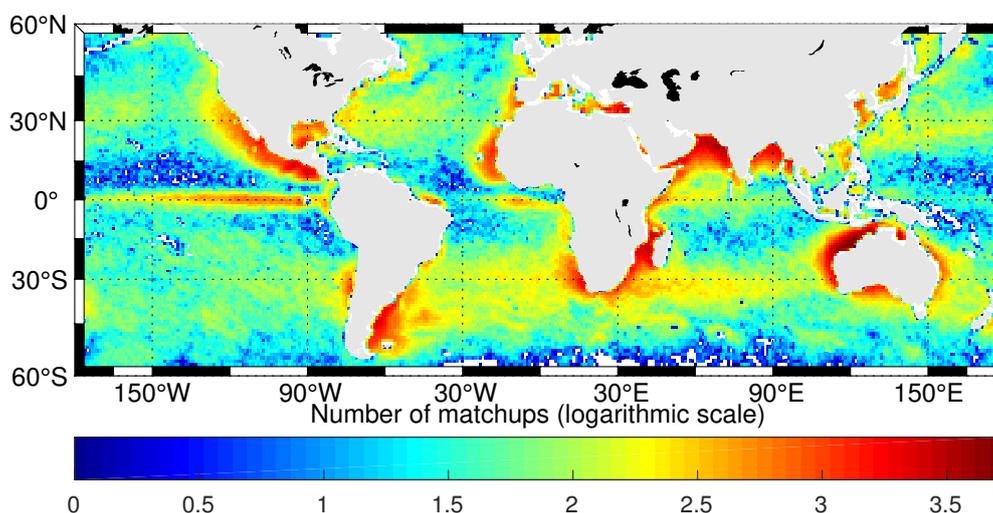
175 figure is
176 region t

Figure 4. Number of collocations. The distribution of collocations is a combination of where the MODIS and AMSR-E data are both present, and this is reflected by the higher number of collocations in clear sky region.

177 Finally, the matchup dataset also contains additional information about the AMSR-E SST pixel: cell
178 position, longitude coordinates and the retrieval time, allowing for stratification of the results based
179 on these parameters.

3.2. Footprint estimation approach

181 To determine the AMSR-E SST footprint, we adopt a linear least-square method as described below,
182 although other methods [19] may also be used. The method exploits the availability of cloud-free
183 high-resolution MODIS SST data, considered as the true sub-resolution SSTs, that overlap each AMSR-E
184 measurement. Consider an AMSR-E SST pixel as shown in Fig. 2. The 25×31 4×4 pixel averages of the
185 original MODIS L2 SST field centered on the AMSR-E field-of-view, are displayed as red squares in the
186 figure and the theoretical field-of-view of the AMSR-E 6.93 GHz channel is plotted in black. We express
187 the MODIS pixels as a column vector $M_{775×1}$. We express the AMSR-E pixels also as a column vector
188 A_{Nx1}, where N is the number of matchups used in the analysis. In perfect conditions (absence of
189 measurement noises), the coarse-resolution AMSR-E SST measurement results from a weighted average

of the sub-resolution SSTs (approximated here by the MODIS measurements). In this ideal case, the relation between the collection of all available AMSR-E SST pixel measurements (A) and MODIS machups (M), can be written as:

$$
\begin{pmatrix} a_1 \\ a_2 \\ a_3 \\ a_4 \\ \vdots \\ a_{N-1} \\ a_N \end{pmatrix}_A = \begin{pmatrix} m_1^1 & m_2^1 & m_3^1 & \cdots & m_{775}^1 \\ m_1^2 & m_2^2 & m_3^2 & \cdots & m_{775}^2 \\ m_1^3 & m_2^3 & m_3^3 & \cdots & m_{775}^3 \\ m_1^4 & m_2^4 & m_3^4 & \cdots & m_{775}^4 \\ & & & \vdots & \\ m_1^{N-1} & m_2^{N-1} & m_3^{N-1} & \cdots & m_{775}^{N-1} \\ m_1^N & m_2^N & m_3^N & \cdots & m_{775}^N \end{pmatrix}_M \begin{pmatrix} h_1 \\ h_2 \\ h_3 \\ \vdots \\ h_{775} \end{pmatrix}_H
\tag{1}
$$

or more compactly as:

$$
A_{N \times 1} = M_{775 \times N} H_{775 x 1}
\tag{2}
$$

where H is the footprint vector containing the weighting elements. A more realistic representation, i.e., one including AMSR-E measurement noise ϵ, can be written as:

$$
A_{N \times 1} = M_{775 \times N} H_{775 x 1} + \epsilon_{N \times 1}
\tag{3}
$$

Eq. 3 simply identifies a regression relation between A and M; i.e., the SST of every AMSR-E pixel is seen to be the H-weighted average of the sub-resolution MODIS SSTs. The problem of deriving the AMSR-E footprint is then equivalent to determining the correct form of H, which minimizes the following difference:

$$
\arg \min_H \| M_{775 \times N} H_{775 x 1} - A_{N \times 1} \|_2^2
\tag{4}
$$

This is the standard linear least-square problem, and there are several methods [20] for solving this type of problem. However, the solution to this problem allows for both positive and negative values of the elements of H, but it is unlikely that any of the regions in the AMSR-E field-of-view have a negative weight, this would be equivalent to a negative number of photons arriving at the detector from the region. We therefore add the constraint that all elements of H must be positive:

$$
H_i \geq 0, \quad \forall i = 1, \cdots 775
\tag{5}
$$

In addition, assuming that there is no bias between the AMSR-E field and the MODIS field, the elements of H should sum to one to preserve the mean value of the AMSR-E SST pixel – the temperature of an AMSR-E SST retrieval from a uniform field should be the temperature of the field. To facilitate the analysis, we fold any bias between the retrievals into the error term of Eqn. 3 and apply the following constraint:

$$
\sum_{i=1}^{i=775} H_i = 1
\tag{6}
$$

Subject to these constraints our least squares problem becomes:

$$
\arg \min_H \| M_{775 \times N} H_{775 x 1} - A_{N \times 1} \|_2^2 \quad \text{Subject to} \quad \sum_{i=1}^{i=775} H = 1 \quad \& \quad H_i \geq 0 \quad (\forall i = 1, \cdots 775)
\tag{7}
$$

209 We used the Matlab solver, *lsqlin*, to determine H subject to the given constraints and the known
210 values A (AMSR-E SST pixels) and M (the corresponding MODIS pixels). As previously noted, the
211 infrared MODIS SST data are used as a proxy for the ground truth. A feature of this approach is that
212 the infrared satellite data are generally contaminated by different noise types [18]. The MODIS SST
213 measurement model for the machup data used here can be expressed as

$$M_{775 \times N} = M^{true}_{775 \times N} + \phi_{775 \times N} \tag{8}$$

214 where M^{true} are the true values of SST and ϕ is the measurement noise. The major sources of noise
215 for the infrared MODIS SSTs are atmospheric contamination, which is long wavelength, and instrument
216 noise and the classification errors (e.g., cloud-contaminated pixels passing as clear pixels), which tend
217 to be short wavelength. The long wavelength error, associated with atmospheric contamination, will
218 contribute to the bias, which has already been folded into the error term and the short wavelength
219 error will average to very nearly zero over the AMSR-E footprint. But, even if it doesn't, it will again
220 just contribute to the error term of Eqn. 3.

221 Because measurement noise and errors are unavoidable in practice, we adopt a bootstrap
222 sampling procedure to solve Eqn. 7. Let $(\tilde{A}^1_{n,1}, \tilde{M}^1_{775 \times n})$, $(\tilde{A}^2_{n,1}, \tilde{M}^2_{775 \times n})$, $\cdots$, $(\tilde{A}^R_{n,1}, \tilde{M}^R_{775 \times n})$ be sets of
223 samples obtained from $(A_{N,1}, M_{775 \times N})$ with $n \lll N$. The elements of each set are drawn uniformly
224 and independently, without replacement, from $A_{N,1}$. For each of the bootstrap samples, we solve
225 Eqn. 7 using the reduced matchup dataset. The resulting footprint is then obtained by averaging the
226 individual bootstrap solutions. The following pseudo-code illustrates the scheme:

---

input : $A_{N,1}, M_{775 \times N}, R, n$
output: $H_{25 \times 35}$(footprint)
1 $H \leftarrow 0$
2 **for** $k \leftarrow 1$ **to** R **do**
3 $\quad$ Sample bootstrapped dataset $(\tilde{A}_{n,1}, \tilde{M}_{775,n})$ from $(A_{N,1}, M_{N,775})$;
4 $\quad$ solve $H^{(k)} = \arg\min\limits_{H}\|\tilde{M}_{775 \times n}H_{775x1} - \tilde{A}_{n \times 1}\|^2_2$ subject to $\sum H = 1$ $\quad$ & $\quad$ $H \geq 0$;
5 $\quad$ $H \leftarrow H + H^{(k)}$
6 **end**
7 $H \leftarrow H/R$;

Algorithm 1: AMSR-E footprint Algorithm

---

4. Results

4.1. Simulation Study

229 Simulations were undertaken to analyze the performance of the estimation algorithm. The
230 results of these simulations were used to choose R, the number of bootstrap samples, and n, the
231 number of matchups in each sample, when the algorithm was applied to the actual dataset. A simple
232 (but realistic) AMSR-E footprint (referred to as the *imposed footprint* hereafter) is used to generate
233 simulated microwave measurements from 250,000 real high-resolution MODIS patches according to
234 Eqn. 3. The 250,000 patches were randomly selected from the approximately 4 million matchups
235 discussed in Section 3.1, with the actual AMSR-E values being replaced by simulated values. For the
236 imposed footprint, we used an elliptical Gaussian function with its major axis rotated 45° clockwise,
237 about the vertical-axis with an aspect ratio of 1.7 ($\approx$ 74/43) approximating the aspect ratio of the
238 6.93 GHz AMSR-E channel. The footprint is normalized according to Eqns. 5 and 6. Microwave
239 measurements were simulated with Eqn. 3, using MODIS data as the ground truth, to which we added
240 Gaussian white noise with a standard-deviation of 0.2 K. 0.05 K Gaussian white noise was added to
241 the MODIS data in order to simulate the infrared instrument noise; i.e., the original MODIS field was

taken as the true SST field and the simulated AMSR-E and MODIS fields were obtained from the 'true' field. The footprint is then estimated using the method described in section 3.2. Footprints were retrieved for three different sets of parameters $(R; n) = (1; 250,000), (1; 2,000), (2,000; 2,000)$. Fig. 5a shows the imposed footprint, which we aim to reconstruct, used to generate the AMSR-E samples from the MODIS data. The retrieved footprints without bootstrap sampling (i.e., $R = 1$; Figs. 5b and c) are dominated by noise. The results of regularization (bootstrapping procedure; Fig. 5d), show a dramatic decrease in the noise of the retrieved footprint with the rotated Gaussian shape of the imposed footprint emerging clearly. Smoothing the retrieved footprint with a 4×4 moving average further reduces the noise yielding a close facsimile to the imposed footprint (Fig. 6e).
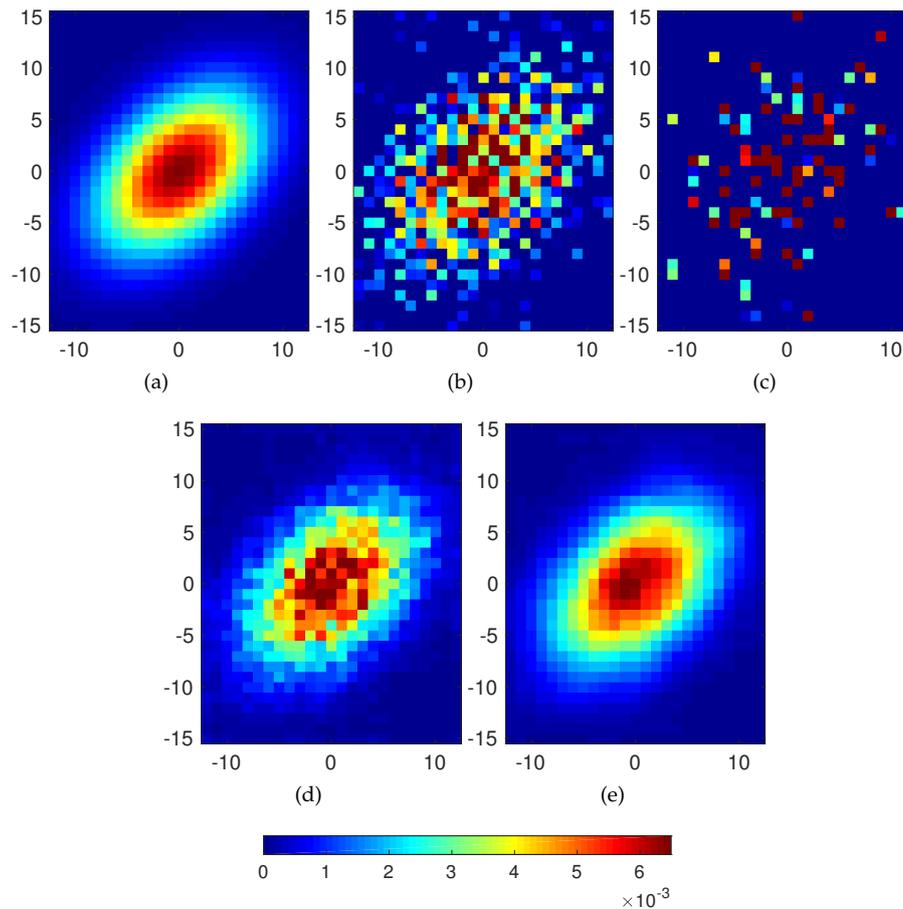
Figure 5. The results using simulated AMSR-E measurements. (a) Imposed footprint, (b) algorithm 1 output with $(R, n) = (1; 250,000)$, (c) $(R, n) = (1; 2,000)$ and (d) $(R, n) = (2,000; 2,000)$. (e) is achieved by applying a 4×4 moving average to (d).

4.2. AMSR-E footprint estimation

In this section we examine the retrieved AMSR-E SST footprint (the SST footprint henceforth to distinguish it from the footprint of individual spectral bands), as a function of AMSR-E cell position, latitude and year. Because the relative angle between the local MODIS coordinate axis and the orientation of the AMSR-E spectral footprint varies with cell position (Fig. 3), the orientation of the SST footprint depends on cell position; hence the decision to retrieve the SST footprint as a function of cell position. A latitudinal dependence could arise from a dependence on the target temperature or on orbital position. Finally, we examined the temporal dependence over the life of the sensor to determine whether or not the footprint changed with time. Recall that SST is determined from a
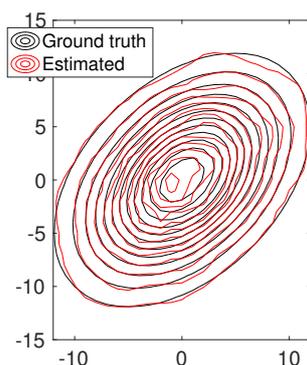
Figure 6. The contour-lines of the imposed footprint (Fig. 5a) and the final result shown in Fig. 5(e).

260 combination of spectral channels and of polarizations for each channel and changes in any of the
261 other channels and/or changes in the characteristics of the other retrieved parameters could impact
262 the SST retrievals.

263 **Cell position dependence.** Matchups were binned by cell position (relative to nadir), with each bin
264 containing a ten position range starting with cell position -115 (-115 to -106, -105 to -96,..., 85 to 94).
265 Samples near the edge of the swath were not included in the analysis as they do not meet the quality
266 criteria specified in Section 2; hence cell position -115 (as opposed to -122) is used as the starting cell
267 position and cell position 96 (as opposed to 122) as the ending number. The reason that the binning
268 is not centered on cell position 0, which corresponds to nadir, is because the $0°$ angle between the
269 MODIS and AMSR-E scans occurs at cell position 10, not 0; i.e., because the rotation axis of the antenna
270 points slightly off nadir. Binning by ten cell positions, provides a suitable number of matchups while
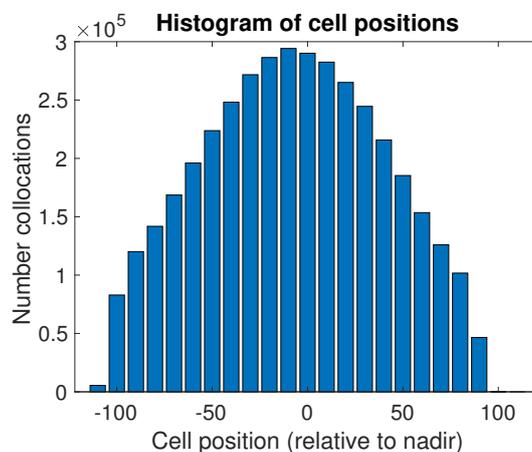271 adequately capturing any cross-track dependence (Fig. 7).

Figure 7. Histogram of the cell positions for the matchups used in this paper.

272 In Fig. 8, we show the empirically derived footprints for each cell position bin. The algorithm
273 characterized by Eq. 7, with $R = 2000$ (number of bootstrap repetitions) and $n = 2000$ (sample size),
274 was applied to the matchup datasets associated with each cell position bin. Only bins involving more
275 than 40,000 matchups were considered (20 bins). The retrieved footprints all suggest a basic elliptical
276 shape but they differ in two key ways. First, the orientation of the ellipses changes with respect to
277 the cell position. Second, as the distance from nadir increases, the footprint becomes narrower in the
278 across-track direction with a concomitant increase in intensity – recall that the weighting function
279 must sum to 1.0 (Eq. 7) so the increase in intensity is consistent with the narrowing of the footprint.
280 The varying rotation angles results from the non-alignment of scan lines of the two sensors shown in
281 Fig. 3. The increase in intensity with distance from nadir results from the concomitant increase in the

across-track spacing and in the size of MODIS pixels. The pixel intensity of the retrieved footprint at a given location is determined by the contribution of the sub-resolution MODIS SST element to the AMSR-E SST at the same location. Consequently, the larger the pixel size the more intense the contribution. Reassuringly, the footprints do not show a significant change in size in the along-track direction.

In the previous paragraph, we found that the retrieved footprint depended on the AMSR-E cell position and on the size of MODIS pixels. In order to remove these dependencies, so that the across-track footprint properties can be better studied and a mean footprint derived, the following correction procedure was undertaken. First, we applied a 4×4 pixel moving average to the across-track footprints (Fig. 8) in order to reduce the pixel-to-pixel noise. We then used the Matlab *griddata* function to transform the MODIS grid (with the x-axis parallel to scan lines, the y-axis parallel to the nadir track and grid spacing in pixels), in which the footprints are produced, to a Euclidean grid in kilometers, aligned with the instantaneous AMSR-E field of view. The results of this procedure are shown in Fig. 9. The transformations applied have clearly removed the cell position dependence of the retrieved footprints, with all of the footprints now generally similar. This is not surprising given that the angle between nadir and the direction to the AMSR-E samples is very nearly independent of cell position. The similarity of the retrieved footprints suggests that a more accurate canonical footprint can be obtained by averaging the footprints of Fig. 9. Fig. 10 presents this average. A significant improvement is observed – the elliptical shape is considerably clearer and much smoother in comparison with the individual footprints. In what follows, the across-track averaged footprint is considered as the reference AMSR-E SST footprint to be used for the latitudinal and temporal analyses. This is also the footprint that we recommend using in other studies requiring knowledge of the characteristics of the AMSR-E SST footprint. To facilitate quantitative comparisons, we render the reference footprint in functional form. Specifically, a curve of the form:

$$
\begin{cases}
f(x,y) = a \exp\left(-\dfrac{1}{2}(A(x-x_0)^2 + B(y-y_0)^2 + C(x-x_0)(y-y_0))\right) \\[2mm]
A = \left(\dfrac{\cos^2(\theta)}{\sigma_x^2} + \dfrac{\sin^2(\theta)}{\sigma_y^2}\right) \\[3mm]
B = \left(\dfrac{\cos^2(\theta)}{\sigma_y^2} + \dfrac{\sin^2(\theta)}{\sigma_x^2}\right) \\[3mm]
C = 2\sin\theta\cos\theta\left(\dfrac{1}{\sigma_x^2} - \dfrac{1}{\sigma_y^2}\right)
\end{cases}
\tag{9}
$$

has been fit, in a least squares sense, to the retrieved mean AMSR-E footprint (Fig. 10). The best fit parameters are: $a = 0.004$, $x_0 = y_0 \approx 0$, $\theta = 1.5736$, $\sigma_x = 0.19$ and $\sigma_y = 0.29$. The fitted model is represented as white contour lines superimposed on the mean footprint in Fig. 10. The parameter $\theta \approx \pi/2$ indicates that the semi-major axis of the retrieved footprint is normal to the local tangent to the AMSR-E scan line. The angles obtained when averaging over bins on one side or the other of the nadir track were not statistically different from $\pi/2$ either.

Latitudinal and temporal dependence. Each of the cell position bin matchup datasets was then binned into four latitudinal bands from 60°S to 45°N. For each of these bins, the across-track footprints were estimated using the procedure described above, normalized and averaged to obtain a footprint for the given latitudinal bin. The retrieved footprints are shown in Fig. 11. Temporal analysis of the footprint was undertaken similarly, except that the cell position bin matchup datasets were binned by year for each year of the 10-year AMSR-E mission (2002 through 2011). The annual across-track averaged footprints are shown in Fig. 12. The number of muchups used to derive the temporal and latitude-based footprints is, of course, reduced compared with number used to obtain the reference footprint, by approximately a factor of four in the latitudinal case and a factor of ten in the annual case, but the resulting footprints are still visually comparable to the reference footprint.
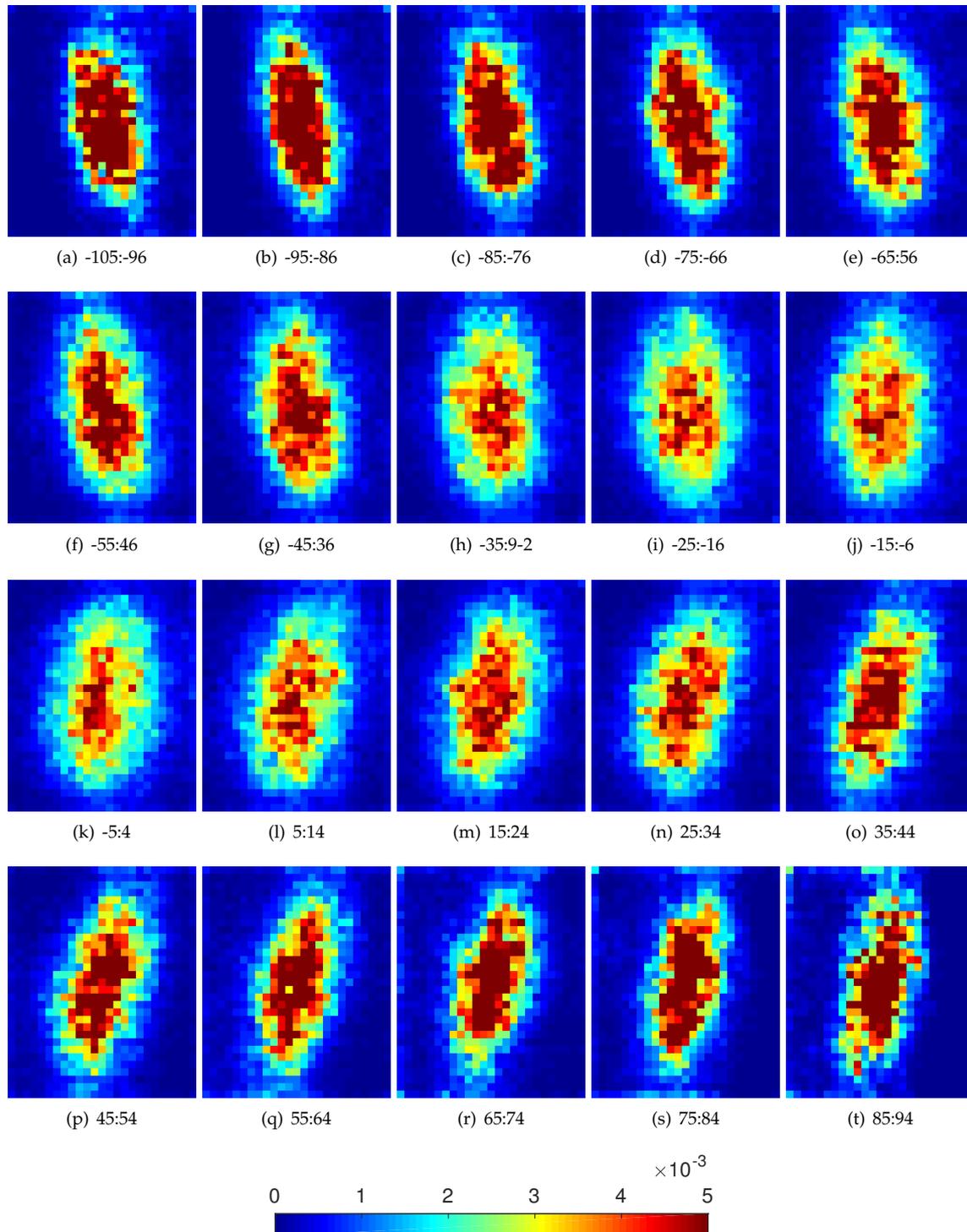
Figure 8. Estimated AMSR-E footprints for different cell positions calculated in the local MODIS grid (no smoothing applied). First bin, -115 to -106, with relatively few matchups (Fig. 7), is not shown.
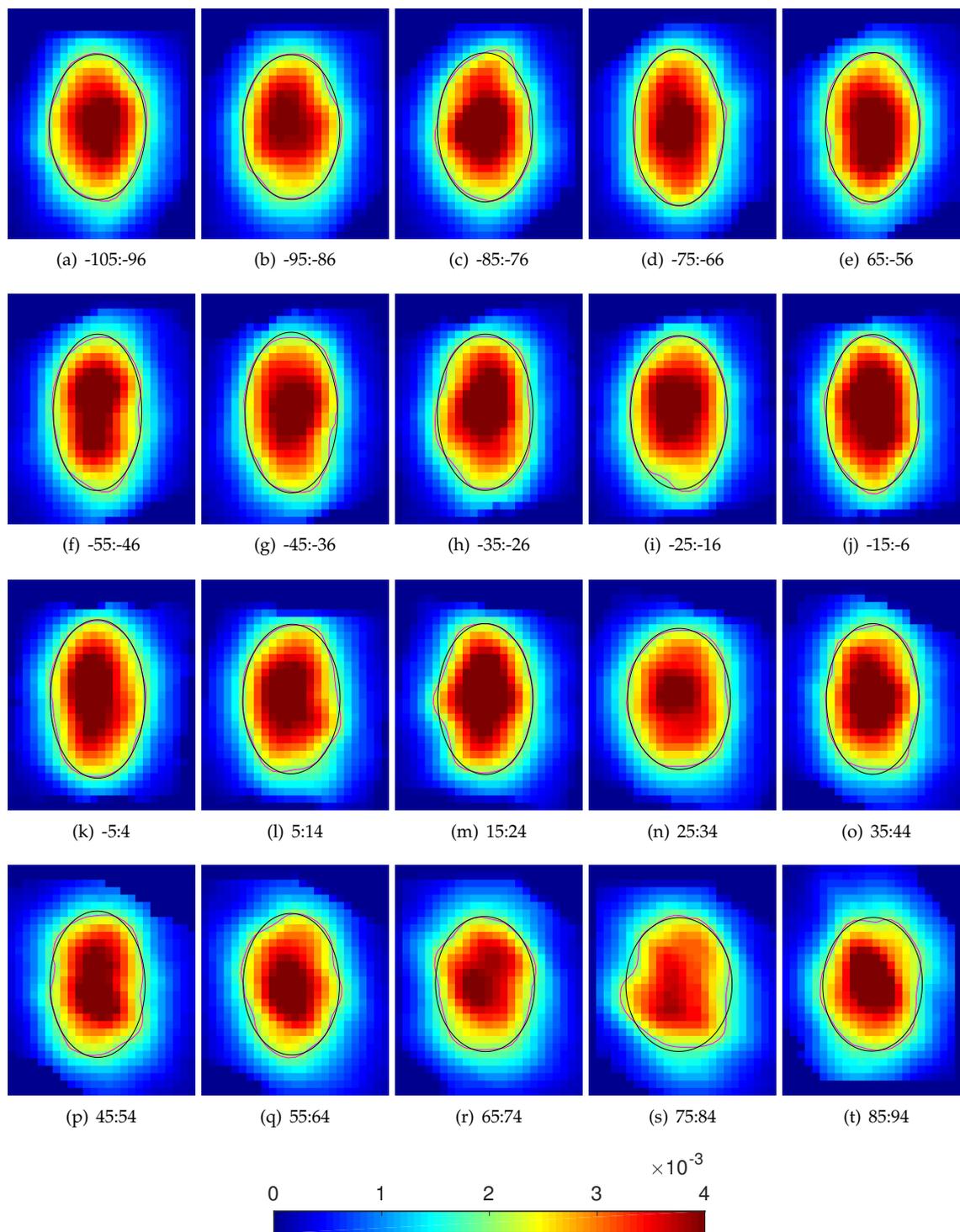
Figure 9. Estimated AMSR-E footprints obtained by projecting the footprints in Fig. 8 on a regularly 4km×4km grid aligned to the instantaneous AMSR-E field-of-view (a 4×4 moving averaged filter was applied prior the calculation). A contour-line at 0.002 level (magenta) and its best fitting ellipse (black) are traced for each footprint.
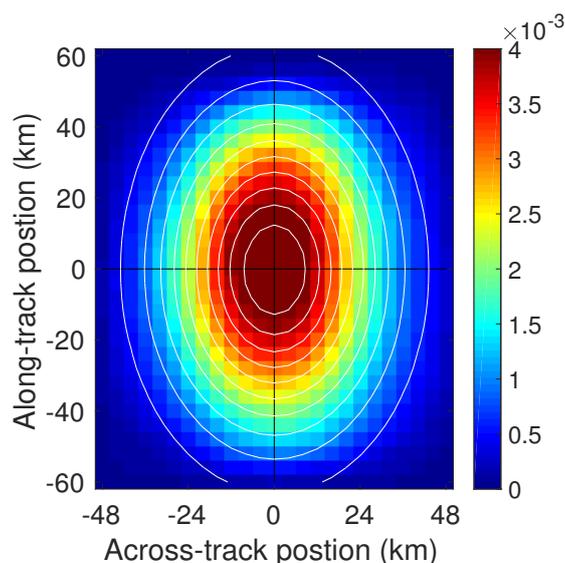
Figure 10. AMSR-E footprint obtained by averaging the across-track footprints shown in Fig. 8. Contour-lines of the fitted analytic model (Eq. 9) are superimposed and plotted in white color.

321 **Statistical comparisons.** In order to quantitatively compare the dependence of the footprint on cell
322 position, latitude and year, we use two different statistics, one based on the Mean Absolute Percentage
323 Error (MAPE), a measure of the accuracy as a percentage, and the other based on the aspect ratio of
324 the best fit ellipse to the footprint, a measure of the accuracy based on shape. Both sets of statistics
325 were determined for the footprints shown in Figs. 9 (cell position), 11 (latitude) and 12 (year). We
326 begin with the MAPE statistic, defined as follows:

$$\text{MAPE} = \frac{\sum_{i=1}^{775}(|f(i) - \hat{f}(i))/\hat{f}(i)|)}{775} \times 100(\%) \tag{10}$$

327 where f is the footprint to evaluate (e.g., retrieved at a particular cell position) and $\hat{f}$ is the reference
328 footprint, depicted in Fig. 10. (MAPE was chosen as one of the two statistics because of the ease in
329 interpreting it. Possible issues with very small values contributing an outsized share to MAPE were
330 reduced by excluding the border of the footprint, where the weights are very low, before estimating
331 it.) The results are shown in Fig. 13a for the across-track dependence, Fig. 13b for annual dependence
332 and Fig. 13c for the latitudinal dependence. In all cases, the amplitude of the errors is below 17%. The
333 errors are found to be smaller for the year-by-year estimates. This was expected considering that the
334 footprints correspond to an average over all the cell positions. The best yearly MAPE value is around
335 6% with an average of $\approx$ 8%. The latitudinal footprints also result from across-track averaging but
336 the associated errors show more variability. This may be due to the variability in the SST fields; the
337 smoother the field the larger the error of the retrieved footprint since the approach used here is not
338 able to obtain an estimate of the footprint from a flat field. SST fields equatorward of $30°N/S$ tend to be
339 more uniform that those in the subtropics. The across-track MAPE results tend to be relatively stable
340 for negative cell positions and show an increasing trend with the increasing positive cell positions.
341 This may result from the sensitivity of the method to the machup size. The number of matchups used
342 to derive the footprints decreases to lower than one-third of the nadir value near the swath edge.
343 This could explain the relatively large errors for high cell positions. However, this argument cannot
344 explain the relatively stable error rates for the negative cell positions. The reason for this is not clear.
345   The second method for comparing footprints is based on the aspect ratio of the footprint
346 determined as follows. For each estimated footprint, we extracted the 0.002 contour-line (magenta
347 curves in Fig. 9 for the along-scan footprints). An ellipse was then least squares fitted to the extracted
348 contour (black curves in Fig. 9) and the aspect ratio, σ_1/σ_2, of this ellipse was calculated, where

σ_1 is the length of the semi-major axis and σ_2 that of the semi-minor axis. The 0.002 contour line used in these fits corresponds to one half of the maximum value of the mean footprint (half of the fitted value of a in Eqn. 9). The same procedure, applied to the mean footprint (Fig. 10), resulted in an aspect ratio of 1.58; somewhat smaller than the 1.7 value of the AMSR-E 6.93 GHz bands. Fig. 14 shows the aspect ratio by (a) cell position, (b) year and (c) latitude. The footprint is stable for the entire mission at approximately the value of the reference footprint. There also appears to be little latitudinal dependence. By contrast, the cell position plot suggests a trend from one side of nadir to the other. This comes as a surprise.

(a) 60°S : 45°S　　(b) 45°S : 15°S　　(c) 15°S : 15°N　　(d) 15°N : 45°N
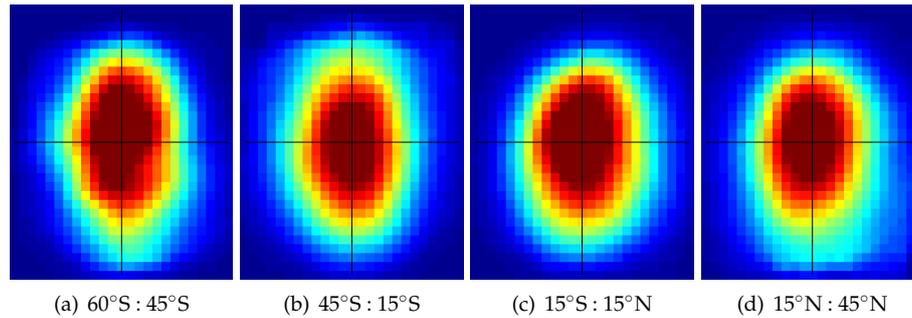
Figure 11. Footprints representing across-track averages in four latitude bins. The color bar, x-axis and y-axis are the same as Fig. 10.

(a) 2002　　(b) 2003　　(c) 2004　　(d) 2005　　(e) 2006

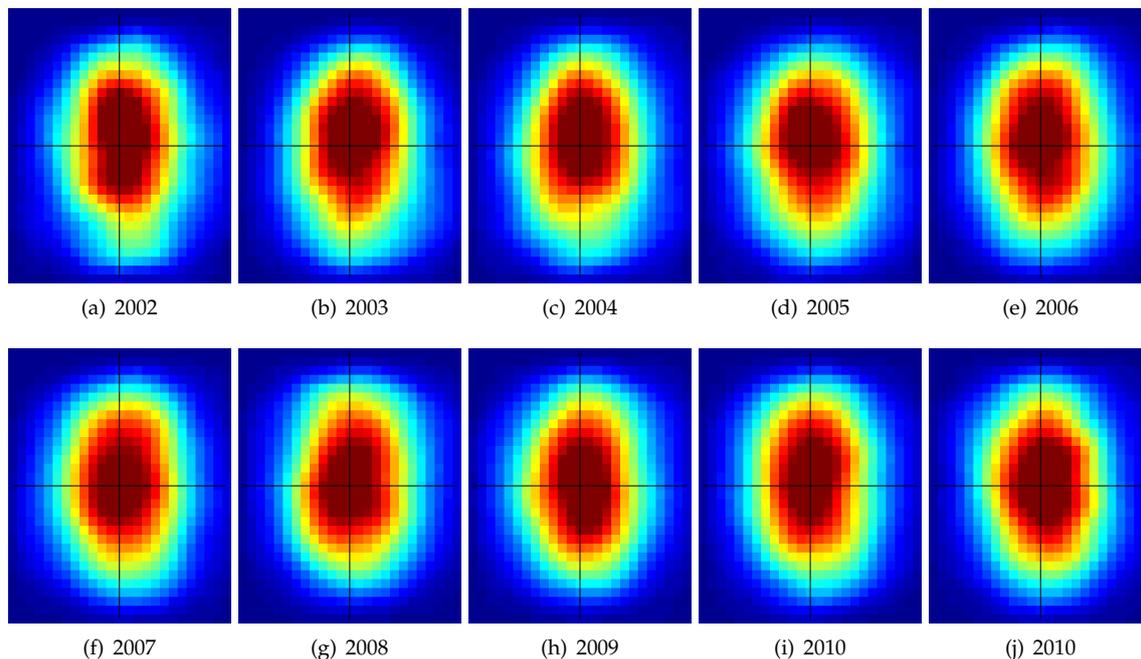(f) 2007　　(g) 2008　　(h) 2009　　(i) 2010　　(j) 2010

Figure 12. Year-by-year estimates of the across-track average footprints. The color bar, x-axis and y-axis are the same as Fig. 10.

5. Discussion

The reference footprint, obtained by averaging the retrievals across all the cell positions, is surprisingly close to the 6.93 GHz band, this despite the inclusion of data from other spectral bands and additional processing. This footprint is robust through time as well as a function of latitude,
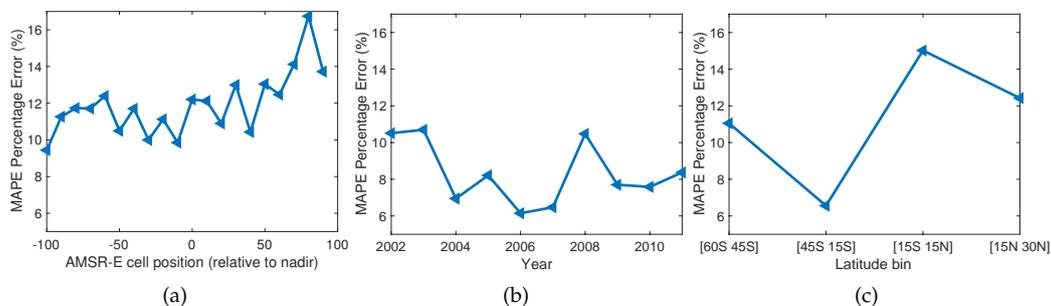
Figure 13. MAPE Percentage Error for (a) across-track, (b) year-by-year and (c) latitude-based footprint estimates.
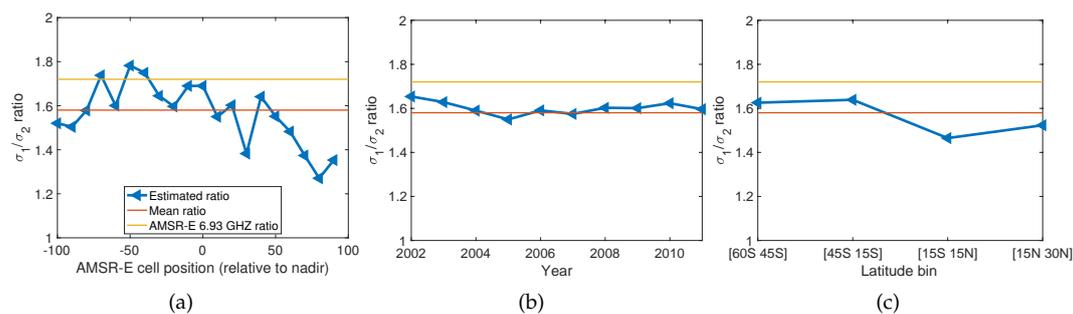

Figure 14. The σ_1/σ_2 aspect ratio of the fitted ellipse to the 0.002 contour-line of the (a) across-track footprints shown in Fig. 9, year-by-year shown in Fig. 12 and (c) those calculated as a function of latitude in Fig. 11. The mean aspect ratio value corresponding to the ellipse fitted to the footprint shown in Fig. 10 is plotted in red. The theoretical value corresponding to the 6.93 GHz channel aspect ratio is plotted in yellow (≈ 1.7).

suggesting that it is a good first choice for the SST footprint where the shape and size of the footprint is relevant.

In order to demonstrate the importance of properly representing the AMSR-E SST footprint, we compare an AMSR-E SST field minus the coincident MODIS SST field, assuming a $56 \times 56\,\text{km}^2$ AMSR-E footprint, with the same difference, assuming the footprint represented by Fig. 10. The criteria used to select the field was that it be largely cloud free and that there be some structure in it - the shape of the footprint is irrelevant when comparing retrievals from different sensors for a uniform field. To difference the fields, it is necessary to map them to the same grid. In this case, the MODIS data were mapped to the AMSR-E field. Specifically, for each AMSR-E pixel, all L2 MODIS SST values falling within the "footprint" of the AMSR-E pixel were averaged. The AMSR-E field is shown in Fig. 15a. The MODIS field, averaged to the AMSR-E field using the $56 \times 56\,\text{km}$ square footprint, is shown in Fig. 15b and the MODIS field, averaged to the AMSR-E field using the footprint of Fig. 10 is shown in Fig. 15c. The difference field for the $56 \times 56\,\text{km}$ footprint is shown in Fig. 15d and that for the footprint of Fig. 10 is shown in Fig. 15e. The difference field associated with the $56\,\text{km}$ footprint shows structure not in that associated with the footprint of Fig. 10.
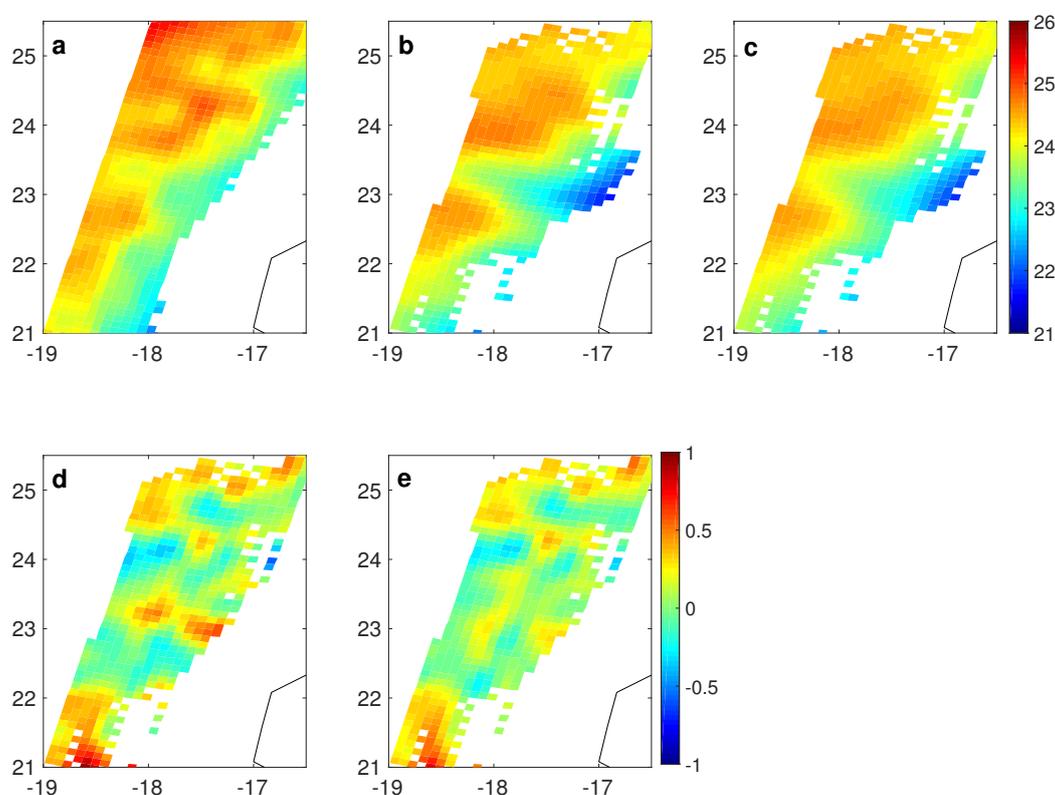

Figure 15. Comparaison of (a) an AMSR-E SST field with the coincident MODIS SST field assuming (b) a $56 \times 56\,\text{km}^2$ footprint, and (c) assuming the footprint represented by Fig. 10. The AMSR-E SST field minus the two MODIS derived fields are, respectively, shown in (d) and (e).

Finally, although we obtained the AMSR-E SST footprint through use of the simultaneous MODIS SST product, we do not believe that the simultaneity of the observations is critical. One could use SST products from other high resolution infrared sensors as long as the time separating the observations is less than six hours. The important consideration here is to avoid times when the surface temperature is changing rapidly, specifically during daylight hours hence the six hour constraint. There must, of course, also be a large number of matchups with whatever sensor is being used to obtain the footprint.

6. Conclusion

The constraint least square method has been applied to a large AMSR-E-MODIS matchup dataset to estimate the footprint (the weights of sub-resolution pixels within a given pixel) of the L2 AMSR-E SST product produced by Remote Sensing Systems. This was done based on the higher resolution L2 MODIS SST dataset (coincident in space and time with the AMSR-E dataset) produced by NASA's Ocean Biology Processing Group. Bootstrapping (bagging) was used to reduce the noise of the retrieved footprint.

The analysis was undertaken as a function of the AMSR-E cell position. The footprint orientation with regard to the nadir track and the size of the pixel was found to vary with distance from nadir. This was due to the angle between the local tangent to the AMSR-E scan-line and to the size of the pixel, both of which increase away from nadir. Once recast into a coordinate system with axes parallel and normal to the local tangent, the across-track footprint was shown to be independent of cell position and the resulting footprints were averaged to obtain a reference footprint, an elliptic Gaussian-like kernel with an aspect ratio of 1.58. This aspect ratio is similar to the that of the AMSR-E 6.95 GHz channel, 1.7.

Temporal and latitudinal analyses were also undertaken and the footprint was found to be independent of these parameters as well.

These results suggest that careful application of the reference footprint when comparing datasets should result in a reduction of root mean square differences over the use of the often quoted 56 × 56 km AMSR-E SST footprint. The reference footprint is also the appropriate footprint to use in the deconvolution of the heaviliy oversampled AMSR-E SST dataset.

7. Data availability

The reference footprint determined in this study is available at: http://www.sstfronts.org.

Author Contributions: BB performed the analysis and wrote the original draft of the manuscript. PC contributed significantly to the writing of the manuscript. BB, PC and GP conceived the study and all contributed to the theoretical aspects of the analysis. CG provided support related to the details of AMSR-E and the processing of AMSR-E brightness temperatures to SST.

Conflicts of Interest: The authors declare no conflict of interest.

Bibliography

1. GCOS. Systematic observation requirements for satellite-based products for climate-Supplemental details to the satellite-based component of the "Implementation Plan for the Global Observing System for Climate in Support of the UNFCCC". *Technical Report GCOS-107, WMO/TD No 1338* **2006**.

2. Chelton, D.B.; Wentz, F.J. Global Microwave Satellite Observations of Sea Surface Temperature for Numerical Weather Prediction and Climate Research. *Bulletin of the American Meteorological Society* **2005**, *86*, 1097–1116, [https://doi.org/10.1175/BAMS-86-8-1097].

3. Parkinson, C.L. Aqua: An Earth-observing satellite mission to examine water and other climate variables. *IEEE Transactions on Geoscience and Remote Sensing* **2003**, *41*, 173–183.

4. O'Carroll, A.G.; Eyre, J.R.; Saunders, R.W. Three-Way Error Analysis between AATSR, AMSR-E, and In Situ Sea Surface Temperature Observations. *Journal Of Atmospheric And Oceanic Technology* **2008**, *25*, 1197–1207.

5. Lean, K.; Saunders, R.W. Validation of the ATSR Reprocessing for Climate (ARC) Dataset Using Data from Drifting Buoys and a Three-Way Error Analysis. *Journal of Climate* **2013**, *26*, 4758–4772.

6. Gentemann, C.L. Three way validation of MODIS and AMSR-E sea surface temperatures. *Journal Of Geophysical Research* **2014**, *119*, 2583–2598.

7. Deschamps, P.Y.; Frouin, R.; CréPon, M. Sea surface temperatures of the coastal zones of France observed by the HCMM satellite. *Journal Of Geophysical Research* **1984**, *89*, 8123–8149.

8. Callies, J.; Ferrari, R. Interpreting Energy and Tracer Spectra of Upper-Ocean Turbulence in the Submesoscale Range (1–200 km). *Journal of Physical Oceanography* **2013**, *43*, 2456–2474.

9. Gambardella, A.; Migliaccio, M. On the superresolution of microwave scanning radiometer measurements. *IEEE Geoscience and Remote Sensing Letters* **2008**, *5*, 796–800.

10. Wentz, F.J.; Gentemann, C.; Smith, D.; Chelton, D. Satellite Measurements of Sea Surface Temperature Through Clouds. *Science* **2000**, *288*, 847–850, [http://science.sciencemag.org/content/288/5467/847.full.pdf].

11. JAXA, A.E. Data Users Handbook. *Saitama, Japan: JAXA Earth Observation Center* **2006**.

12. JAXA. *AMSR-E – AMSR-E Data Users Handbook.* Japan Aerospace Exploration Agency, 2006.

13. Meyer-Lerbs, L. Gridding of AMSR-E Satellite Data. *Master thesis* **2005**, [http://www.iup.uni-bremen.de/PEP_master_thesis/thesis_2005/Thesis_LotharMeyer-Lerbs.pdf].

14. Wentz, F.J.; Meissner, T. Supplement 1 algorithm theoretical basis document for AMSR-E ocean algorithms. *NASA: Santa Rosa, CA, USA* **2007**.

15. Ocean Biology Processing Group, NASA Goddard Space Flight Center, Ocean Ecology Laboratory. Moderate-resolution Imaging Spectroradiometer (MODIS) Aqua Sea Surface Temperature Data; 2014 Reprocessing, 2014. doi: 10.5067/AQUA/MODIS/L2/SST/2014.

16. Walton, C.C. Nonlinear multichannel algorithms for estimating sea surface temperature with AVHRR satellite data. *Journal of Applied Meteorology* **1988**, *27*, 115–124.

17. Franz, B. Implementation of SST Processing within the OBPG. [https://oceancolor.gsfc.nasa.gov/docs/modis_sst/].

18. Wu, F.; Cornillon, P.; Boussidi, B.; Guan, L. Determining the Pixel-to-Pixel Uncertainty in Satellite-Derived SST Fields. *Remote Sensing* **2017**, *9*, 877.

19. Park, T.; Casella, G. The bayesian lasso. *Journal of the American Statistical Association* **2008**, *103*, 681–686.

20. Gill, P.E.; Murray, W.; Wright, M.H. Practical optimization **1981**.

AMSR-E Advanced Microwave Scanning Radiometer - EOS
ECV Essential Climate Variable
JAXA Japan Aerospace Exploration Agency
MODIS MODerate-resolution Imaging Spectroradiometer
NASA National Aeronautics and Space Administration
NASDA National Space Development Agency (Japan)
OBPG Ocean Biology Processing Group
RFI radio frequency interference
RSS Remote Sensing Systems
SST sea surface temperature
WS wind speed